AGU PUBLICATIONS

JGR

Journal of Geophysical Research: Oceans

RESEARCH ARTICLE

10.1002/2014JC010179

Key Points:
- Low-frequency motions on the reef flat are excited by breakpoint forcing
- Bispectral estimates indicate the presence of energetic incident bound waves
- Breaking sea and swell waves work against the incident bound waves

Correspondence to:
J. M. Becker,
jbecker@soest.hawaii.edu

Citation:
Péquignet, A.-C. N., J. M. Becker, and M. A. Merrifield (2014), Energy transfer between wind waves and low-frequency oscillations on a fringing reef, Ipan, Guam, *J. Geophys. Res. Oceans*, *119*, 6709–6724, doi:10.1002/2014JC010179.

Received 21 MAY 2014
Accepted 9 SEP 2014
Accepted article online 15 SEP 2014
Published online 9 OCT 2014

Energy transfer between wind waves and low-frequency oscillations on a fringing reef, Ipan, Guam

Anne-Christine N. Péquignet[1], Janet M. Becker[2], and Mark A. Merrifield[3]

[1]School of Civil, Environmental and Mining Engineering, University of Western Australia, Crawley, Western Australia, Australia, [2]Department of Geology and Geophysics, University of Hawaii at Manoa, Honolulu, Hawaii, USA, [3]Department of Oceanography, University of Hawaii at Manoa, Honolulu, Hawaii, USA

Abstract Field observations from a Guam fringing reef are used to examine the cross-reef energy exchange between high-frequency sea and swell (SS) and low-frequency infragravity (IG) and far infragravity (fIG) waves. Energetic SS waves (significant wave heights 2–4 m) break at the outer reef, leading to weak (<1 m) conditions on the shallow reef flat. As SS waves shoal on the reef face before breaking, IG and fIG energy fluxes both increase through nonlinear energy transfer from the SS waves. In contrast, through the surf zone, the IG energy flux decreases whereas fIG flux increases. The decrease in IG energy flux through the surf zone is attributed to breaking SS waves working against the incident bound IG wave energy, which dominates breakpoint forced IG waves, yielding a net flux decrease. In contrast, fIG energy flux increases through the surf zone, consistent with breakpoint forcing and the absence of an energetic bound fIG component on the reef face. IG and fIG energy fluxes decay on the shallow reef flat due primarily to frictional dissipation, with tidal modulations attributed to nonlinear conversion and friction. Forcing at fIG frequencies may lead to a normal mode response on the reef with comparable incoming and outgoing fIG energy fluxes at the outer reef flat, depending on water level over the reef flat and the degree of frictional dissipation.

1. Introduction

Low-frequency (LF) waves, at infragravity (IG) ($0.005 < f < 0.05$ Hz) and far infragravity (fIG) ($0.001 < f < 0.005$ Hz) frequencies, are prevalent over fringing coral reef platforms [*Roberts et al.*, 1992; *Hardy and Young*, 1996; *Kench*, 1998; *Lugo-Fernández et al.*, 1998; *Péquignet et al.*, 2009; *Pomeroy et al.*, 2012; *Monismith et al.*, 2013]. They have been found to contribute significantly to bed stresses [*Van Dongeren et al.*, 2013], shoreline inundation [*Ford et al.*, 2013], and horizontal current and water level variability [*Péquignet et al.*, 2009] over reefs. In general, LF energy increases through the surf zone of fringing reefs as wind wave energy in the sea and swell (SS) frequency band (defined here as $0.05 < f < 0.2$ Hz) decreases [*Pomeroy et al.*, 2012], representing a nonlinear energy transfer from high to low frequencies. SS waves dissipate primarily due to breaking, which for steep fringing reef faces tends to occur in a localized breaker zone near the reef edge. Bottom friction provides an additional dissipation mechanism particularly as reef substrate tends to be significantly rougher than sand, although reef flat platforms can be relatively smooth [*Péquignet et al.*, 2009]. SS breaking at the outer reef favors the establishment of cross-shore standing or partially standing LF waves [*Nakaza and Hino*, 1991; *Lugo-Fernández et al.*, 1998]. At Ipan, Guam, LF standing modes have been observed across a fringing reef flat during large wave conditions associated with tropical storm Man-Yi [*Péquignet et al.*, 2009]. Laboratory experiments and numerical simulations also show that time-varying breaking SS waves (i.e., wave groups) generate significant LF energy [*Nakaza and Hino*, 1991; *Karunarathna and Tanimoto*, 1995; *Demirbilek et al.*, 2007; *Nwogu and Demirbilek*, 2010; *Sheremet et al.*, 2011].

SS waves may force IG motions through (1) nonlinear interactions that transfer energy from SS waves to bound and free IG waves and (2) variable breakpoint forcing in the surf zone. The first mechanism consists of quadratic difference interactions between waves in the SS frequency band. Quadratic phase coupling of two SS waves with frequency f_1 and f_2 may result in a nonlinear triad interaction generating a third wave of difference (and sum) frequency $f_3 = f_1 \pm f_2$ and wave number $k_3 = k_1 \pm k_2$. In deep and intermediate water depths, these second-order, or bound, waves at the difference frequency do not satisfy the local dispersion relationship and are phase locked to the primary waves. *Longuet-Higgins and Stewart* [1962] showed that the radiation stress gradient associated with the SS wave group forces the second-order bound waves. For

a wavefield with small Ursell number and horizontally uniform statistics [*Hasselmann et al*., 1963], the bound wave is 180° out of phase with the SS wave group. As the waves shoal to shallower depths, a phase lag develops between the bound wave and the incident wave group, which allows for the transfer of energy between the SS waves and the bound wave response [*Masselink*, 1995; *Janssen et al*., 2003; *Van Dongeren et al*., 2003]. *Battjes et al*. [2004] described both the frequency and spatial variation of the phase shift between the SS envelope and the bound waves and showed that the phase shift increases shoreward with decreasing depth allowing for growth of the low-frequency waves until breaking of the SS waves. In shallow water, triad interactions approach resonance and the IG energy peaks at the onset of wave breaking [*Ruessink*, 1998]. In addition, in shallow water, the IG waves form a near-resonant triad and may propagate as free waves toward shore [*Herbers et al*., 1995] where they may reflect and radiate energy back to sea [*Suhayda*, 1974; *Guza and Thornton*, 1985; *Elgar et al*., 1994; *Herbers et al*., 1995; *Sheremet et al*., 2002]. In the surf zone, the high-frequency sum waves are rapidly dissipated, but the difference IG waves often remain and may dominate the spectrum of the swash zone [*Guza and Thornton*, 1982; *Raubenheimer and Guza*, 1996; *Ruggiero et al*., 2004; *Stockdon et al*., 2006]. Some low-frequency energy also may be topographically trapped by refraction and remain along the shore as free edge waves [*Bowen and Guza*, 1978; *Oltman-Shay and Guza*, 1987; *Bryan and Bowen*, 1996; *Bricker et al*., 2007]. A second important mechanism for IG wave generation occurs in the surf zone due to the breaking of SS waves with variable amplitude, resulting in a spatially varying breakpoint and modulated radiation stress gradient forcing. Solving the equations of motion with an idealized forcing term on plane and barred beaches, *Symonds et al*. [1982] and *Symonds and Bowen* [1984] demonstrated how a moving breakpoint generates free waves at the group frequency and its harmonics. In the nearshore, both bound waves and breakpoint generated long waves may contribute to the IG field. *Lippmann et al*. [1997] extended the breakpoint forcing of *Symonds et al*. [1982] to three dimensions and showed theoretically that resonant edge waves may be excited. Following *Phillips* [1977], *Schäffer* [1993] averaged the conservation equations for mass and momentum over a short wave period and obtained a forced second-order longwave equation with the forcing in terms of the short wave radiation stress. The radiation stress is modeled using two approximations to the wave amplitude through the surf zone, which account for breakpoint generated LF waves and the transmission of bound waves released at breaking. *Schäffer* [1993] showed that the two forcing mechanisms have similar orders of magnitude and may work against each other, i.e., wave breaking may extract energy from incident bound waves. *Karunarathna and Tanimoto* [1995] performed numerical experiments for both breaking and nonbreaking wave groups over an idealized reef. For nonbreaking incident wave groups, both bound and free longwaves generated at the reef crest were energetic on the reef flat, while breaking incident wave groups were found to reduce the bound wave energy. Recent observations on Ningaloo reef and numerical simulations [*Pomeroy et al*., 2012; *Van Dongeren et al*., 2013] suggest that breakpoint forcing generates free infragravity wave motions on the steep forereef. Shoaling bound waves largely are dissipated in the surf zone based on numerical simulations [*Pomeroy et al*., 2012].

Significant dissipation of IG waves has been reported in the nearshore both in field measurements [*Sheremet et al*., 2002; *Henderson and Bowen*, 2002; *Lowe et al*., 2005] and in laboratory experiments [e.g., *Baldock et al*., 2000; *Battjes et al*., 2004]. The energy loss has been attributed to bottom friction and nonlinear transfer to higher frequency [*Henderson et al*., 2006; *Thomson et al*., 2006; *Baldock*, 2012], and shoreline breaking [*Van Dongeren et al*., 2007; *de Bakker et al*., 2014]. Recently, *Baldock* [2012] argued that bound waves are not released as a result of short wave breaking but instead are dissipated through nonlinear interactions.

In this paper, field measurements across the fringing reef at Ipan, Guam, during energetic wind wave conditions are used to estimate the contribution of nonlinear processes and friction to the LF energy balance. Section 2 describes the field experiment and section 3 details the methods used to analyze the field observations. In section 4, we present a description of the observed LF energy, assess bound wave contributions using bispectral analysis, evaluate terms in the LF energy balance, and compare the LF wave response at Ipan for the present data set to that observed during the Man-Yi storm event. A discussion and summary follow in section 5.

2. Field Experiment

Data used in this study were collected as part of the Pacific Island Land-Ocean Typhoon (PILOT) project, which was aimed at assessing coastal inundation at reef-fringed islands during large wave events [*Boc*

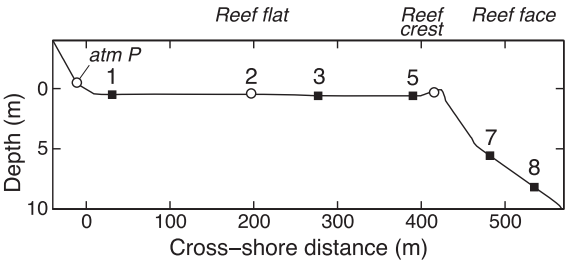

Figure 1. Sensor locations along the cross-shore transect of Ipan reef, with bathymetry specified from Scanning Hydrographic Operational Airborne Lidar Survey (SHOALS) data. Open circles indicate the SBE26plus pressure sensors, and black squares indicate colocated pressure sensors and current meters (ADP). The sensor labeled "atm P" is a single SBE26plus pressure sensor deployed above sea level to measure atmospheric pressure.

et al., 2008]. The study site at Ipan on the south shore of Guam (13.372°N, 144.775°E) has a wide (∼400 m), shallow (<1 m) fringing reef flat, that is approximately uniform in the alongshore direction. A cross-shore array of wave and water level recorders has been maintained at Ipan since August 2005, with different sensors maintained at different locations across the reef flat and reef face during the sequential deployments. The data used in this chapter were collected during the N deployment in September to November 2009. This section of data was chosen because it includes several energetic SS wave events, and the availability of current measurements across the reef allows for the computation of LF energy flux and nonlinear transfer terms.

Nortek Aquadopp Acoustic Doppler Profilers (ADP) and Seabird SBE 26Plus wave and water level recorders were deployed across the reef, with two ADPs offshore of the reef crest and three on the reef flat (Figure 1). The ADPs were deployed horizontally with the transducer ∼5 cm above the bed, and sampled at 1 Hz in segments of 3 h every 4 h, with a single cell size and blanking distance of 0.2 and 0.1 m for reef flat sensors, and 1 and 1 m for reef face sensors. The SBE 26Plus sensors were deployed on the reef flat between the ADPs and one sensor was buried on land to measure atmospheric pressure and potential inundation (sensor atm P, Figure 1). The Seabird sensors sampled at 1 Hz nearly continuously with 20 s gaps every 12 h. Linear wave theory was used to compute sea surface elevation (η) from bottom pressure and surface cross shore (u, positive onshore) and alongshore (v, positive toward the south) currents from the measured velocity. The noise level for the horizontal velocity measurements at 1 Hz sample rate is ∼0.08 m s^{-1} based on manufacturer estimates, which tended to match the noise floor observed in the deep reef face sensors. On the reef flat, the measured noise level tended to be twice as high. Changes in water temperature on the reef account for uncertainties of <0.2% in the estimation of sea surface elevation from the pressure observations. Water level was computed from pressure with an inverse barometer correction. Times when the reef flat sensors were out of the water were flagged and excluded from the analysis. A Datawell directional wave buoy located 2.4 km southeast of the reef array (13.354°N, 144.788°E) at the 200 m isobath provided deep water wave conditions at 30 min intervals. *Péquignet et al*. [2011] provides further details on the field site and data set.

The significant wave height (H_s), peak period (T_p), and dominant wave direction measured offshore (buoy) and on the reef face (8 m depth, 15 min intervals) (Figure 2) show three energetic wave events ($H_s > 3.5$ m) during the N deployment: 14 September with maximum $H_s = 3.7$ m, $T_p \sim 12$ s, and dominant direction ∼60° TN at the buoy, 2 October 2009 with maximum $H_s = 3.9$ m, $T_p \sim 13.6$ s, and dominant direction ∼80° TN, and 15 October with maximum $H_s = 3.6$ m, $T_p \sim 8.3$ s, and dominant direction ∼90° TN. In addition, a smaller event of longer duration was measured from 6 to 8 November with $H_s = 2.5$ m, $T_p \sim 13$ s, and the dominant direction ∼75° TN. The observations are representative of energetic wind wave events that occur regularly during the winter along the east coast of Guam. For the three largest events, the peak in wave height occurred during low tide while for the November event, a range of tidal elevations were sampled, (Figures 2a and 2d). Wave heights reduce considerably between the reef face (sensor 8, which is similar to sensor 7, not shown) and the reef crest (sensor 6) and outer reef flat (sensor 5). We consider the surf break to occur between sensors 7 and the reef crest. All current velocities were rotated such that the cross-shore component, u, is directed along 84° TN, based on the time-averaged direction of the SS and LF energy fluxes at the outer reef flat sensor 5. The events of 14 September, 2 October, and 6–8 November represent swell arrivals unrelated to local meteorological conditions, as measured at the NOAA tide gauge station at Pago Bay (13.428°N, 144.797°E) (Figure 2f). The 15 October event included some local wind forcing and the peak SS energy is at a lower period than the earlier swell events. The energetic wind wave events resulted in large wave setup on the reef flat, reaching 0.9 m at the outer

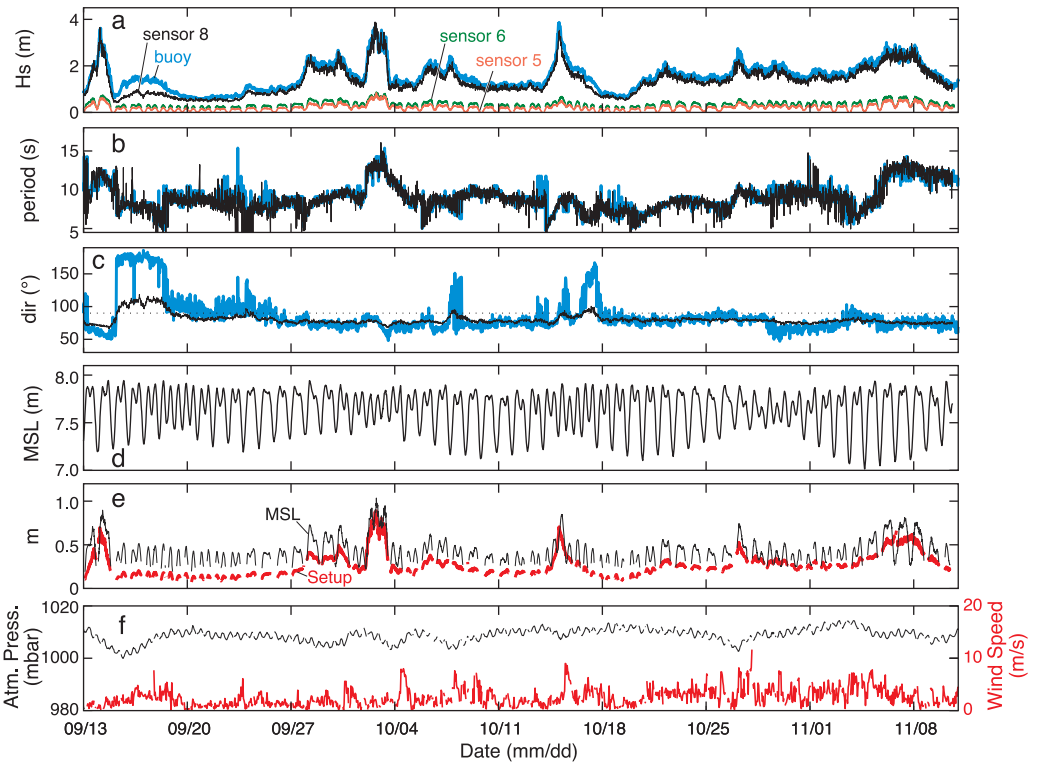

Figure 2. Wave and water level conditions during the experiment, including (a) sea and swell (SS) band significant wave height (H_s) at the offshore buoy, on the reef face (sensor 8) and on the reef flat (5 and 6), (b) the peak SS wave period at the buoy and at 8, (c) the incident SS wave angle (relative to true north) at the buoy and 8, (d) mean sea level (MSL), including mean water depth, at 8, (e) MSL and wave setup on the reef flat (sensor 1), and (f) atmospheric pressure (black) and wind speed (red) observed at the NOAA CO-OPS tide gauge station at Pago Bay.

reef sensor during the 2 October event (Figure 2e). In general, setup on the Ipan reef tends to scale as 0.35 times incident H_{rms} on the reef face [*Vetter et al*., 2010], with higher setup occurring at low tide than high tide for a given incident wave height [*Becker et al*., 2014].

3. Methods

Phillips [1977] and *Schäffer* [1993] present LF energy equations in the time domain assuming a scale separation between the SS and LF motions where the free-surface elevation and the velocity are decomposed as $\eta=\eta'+\zeta, u=u'+U$, the prime indicates the SS component, and ζ and U are the LF components. Here we evaluate the steady, alongshore uniform, weakly nonlinear LF energy balance in the frequency domain following *Henderson et al*. [2006]

$$\frac{\partial F(f)}{\partial x}=W(f)-D(f), \tag{1}$$

where $F(f)$ is the cross-shore energy flux at frequency f,

$$F(f)=g(hC_{\zeta,U}(f)+C_{\zeta,M}(f)+C_{S_{xx},U}(f))\equiv F_1+F_2+F_3, \tag{2}$$

$W(f)$ is the nonlinear transfer of energy to and from f from other frequencies,

$$W(f)=gC_{S_{xx},\frac{\partial U}{\partial x}}(f), \tag{3}$$

and $D(f)$ is the rate of dissipation. In (2) and (3), $C_{X,Y}(f)$ is the cospectrum between X and Y at frequency f, h is the mean water depth, and g is the acceleration due to gravity. The SS volume flux, M, and radiation stress, S_{xx}, are given by

$$M=\eta' u', \qquad S_{xx}=hu'u'/g+\eta'\eta'/2. \tag{4}$$

In section 4.3, we evaluate the energy equation (1) in the form

$$\frac{\partial(F_1(f)+F_2(f))}{\partial x}=W_1(f)-D(f), \tag{5}$$

where

$$W_1(f)=W(f)-\frac{\partial F_3(f)}{\partial x}. \tag{6}$$

An equivalent formulation of (6) is

$$\hat{W}_1(f)=-gC_{U,\frac{\partial S_{xx}}{\partial x}}(f). \tag{7}$$

As discussed by *Battjes et al*. [2004], the nonlinear transfer term (7) may be interpreted as the depth-integrated rate of work of the short wave radiation stress gradient on the LF water motion. For the reef face and outer reef flat sensors impacted by the surf zone, we also evaluate (5) using $\hat{W}_1(f)$ as it appears to capture the radiation stress gradient forcing through the surf zone more directly than (6) given the available sensor spacing.

The time series of the free-surface elevation, η, and cross-shore surface currents, u, are band-pass filtered over the SS frequency band to compute η', u', M and S_{xx} for 3 h records. In (3), $\frac{\partial U}{\partial x}$ is evaluated using the finite difference approximation to the shallow water mass conservation equation between sensors as in *Henderson et al*. [2006]. F, W, and $\hat{W}_1$ (equations (2), (3), and (7)) are estimated from auto and cross spectra involving ζ, U, M, and S_{xx} based on Fourier transforms of the detrended 3 h data segments.

In the linear approximation, following *Sheremet et al*. [2002], we decompose the LF energy in the wavefield

$$E(f)=\frac{g}{2}\left[C_{\zeta,\zeta}(f)+\frac{h}{g}C_{U,U}(f)\right], \tag{8}$$

into shoreward (incoming, + superscript) and seaward (outgoing, − superscript) components

$$E^{\pm}(f)=\frac{g}{4}[C_{\zeta,\zeta}(f)+(h/g)C_{U,U}(f)\pm 2\sqrt{h/g}C_{\zeta,U}(f)], \tag{9}$$

where $C_{X,X}(f)$ is the one-sided autospectrum of X. For near normal propagation, the linear flux associated with the free LF incoming and outgoing waves is given by

$$F_1^{\pm}(f)=\sqrt{gh}E^{\pm}(f). \tag{10}$$

We remark that the shallow water approximation is valid in the LF band at all water depths considered.

The LF dissipative term, $D(f)$ in (1), in each frequency band is calculated following *Henderson and Bowen* [2002]

$$D(f)=c_f(g/h)^{3/2}|\eta|| <\eta>_f|^2, \tag{11}$$

where $|\eta|$ is the total RMS sea surface elevation, $| <\eta>_f|^2$ is the contribution to sea surface elevation variance at LF frequency f, and c_f is the LF bottom drag coefficient. LF wave breaking [*Van Dongeren et al*., 2007] is neglected in the dissipation term.

We present the various energy equation terms in the time domain by summing spectral density estimates over the lG ($0.005 < f < .05$) and flG ($0.001 < f < 0.005$) bands. In what follows, F_i ($i=1-3$), W_1, $\hat{W}_1$, and D are the band-averaged flux, transfer and dissipation (2), (6), (7), and (11). The band-averaged values of (8) and (10) are denoted by E and $F_1^{\pm}$. In (8)–(10), we obtain similar results if $C_{U,U}$ is corrected for measurement noise by subtracting a white spectrum obtained by averaging velocity spectral densities in the 0.4–0.5 Hz frequency range for each 3 h time segment.

Bispectra of the sea surface elevation are computed following [*Herbers et al*., 1994], with triads f_1, f_2, and $f_3=f_1+f_2$ considered. Monte Carlo tests are used to evaluate the significance of the real and imaginary part of the bispectrum relative to signals with randomized phase. We consider bispectral amplitudes to be significant if they exceed the randomized phase bispectrum by two standard deviations.

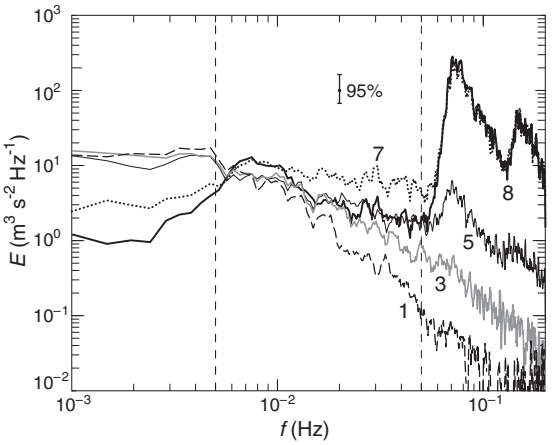

Figure 3. Spectral estimates of energy density from the five current-meter sensors across Ipan reef for the wave event of 2 October 2009, (10-02-16, MM-DD-HH). The vertical dashed lines indicate the fIG and IG frequency bands.

4. Results

4.1. LF Energy Across the Reef

Wave energy across the reef varies with frequency, particularly in the surf zone between the reef face and outer reef flat, as illustrated by spectral comparisons during an energetic wave event (Figure 3). SS energy density decreases by over three orders of magnitude on the reef crest compared to the reef face (sensor 5 compared to 7), due primarily to dissipation associated with wave breaking [*Péquignet et al*., 2011]. Bottom friction largely accounts for the further decay of SS energy on the reef flat [*Péquignet et al*., 2011]. At low frequencies, IG and fIG band energies both increase on the reef face (between sensors 8 and 7). On the shoreward limit of the reef crest (sensor 5), fIG energy increases and IG energy decreases relative to the reef face (sensor 7). fIG energy remains high on the reef flat moving toward shore (sensors 3 and 1), whereas IG energy diminishes shoreward over the reef flat. The distinction between the fIG and IG bands was introduced by *Oltman-Shay et al*. [1989] to differentiate between shear waves in the fIG band, caused by instabilities of longshore current shear, and gravity waves in the IG band. The observed ratio between velocity and pressure variances is $\sim g/h$ during energetic wave events in both the IG and fIG bands at Ipan, which, following *Lippmann et al*. [1999], suggests that fIG variability is associated with gravity waves rather than shear waves. Here we make a distinction between fIG and IG variability because of their different transformation properties across the reef (Figure 3).

The tendency for IG and fIG energy to decrease and increase, respectively, through the surf zone, exhibits a tidal dependence. At low tide during an energetic wave event (MM-DD-HH: 10-02-16), IG energy increases strongly over the reef face, followed by a similar magnitude decrease through the surf zone (Figure 4a). The IG energy then decreases over the reef flat toward shore. During a weaker wave event, IG energy at low tide (11-08-04) exhibits a similar cross-shore variation as the more energetic 2 October event; however, during the preceding high tide, (11-07-20), when IG energy at the deepest sensor was comparable to low tide, the IG energy increases slightly through the surf zone, with a cross-shore energy decay rate over the reef flat similar to low tide and the 2 October event. The tidal dependence of IG energy through the surf zone is presented by comparing the energy on the reef face (sensor 7) to that at the shoreward limit of the reef crest (sensor 5) and colored with the tide h', defined as the detrended mean water level at sensor 8 (Figure 4b) for records with $H_{\{8ss\}} > 1.5$ m. During weak events measured on the reef face ($E_{7IG} < 0.08$), the energy on the outer reef flat (E_{5IG}) is higher at high tides than low tides, and during high tides the energy tends to be higher on the reef flat than on the reef face. At higher IG energy levels, the energy on the outer reef flat is always lower than on the reef face, for all tidal conditions. At fIG frequencies, energy increases through the surf zone (Figure 4c) for the energetic 2 October event and the weaker November events. During the 2 October event, fIG energy continues to increase over the reef flat, whereas during the weaker November events the energy decays, with stronger decay at low tide. Comparing the records with $H_{8ss} > 1.5$ m confirms that fIG energy increases through the surf zone for all wave events, with a tendency for higher energies at high than low tide (Figure 4d).

We next present - estimates of $F_1(f)$ and $F_2(f)$, (2), for each 3 h time segment integrated over the IG frequency band, yielding time series of linear, F_1, and nonlinear, F_2, energy fluxes at each current meter sensor (Figure 5a). The linear flux also is decomposed into incoming (F_1^+) and outgoing ($-F_1^-$) components according to (10). All LF fluxes are weak except during SS wave events (Figure 2a), suggesting that remotely generated, freely propagating IG waves are not prominent. The IG linear fluxes are positive toward shore at each

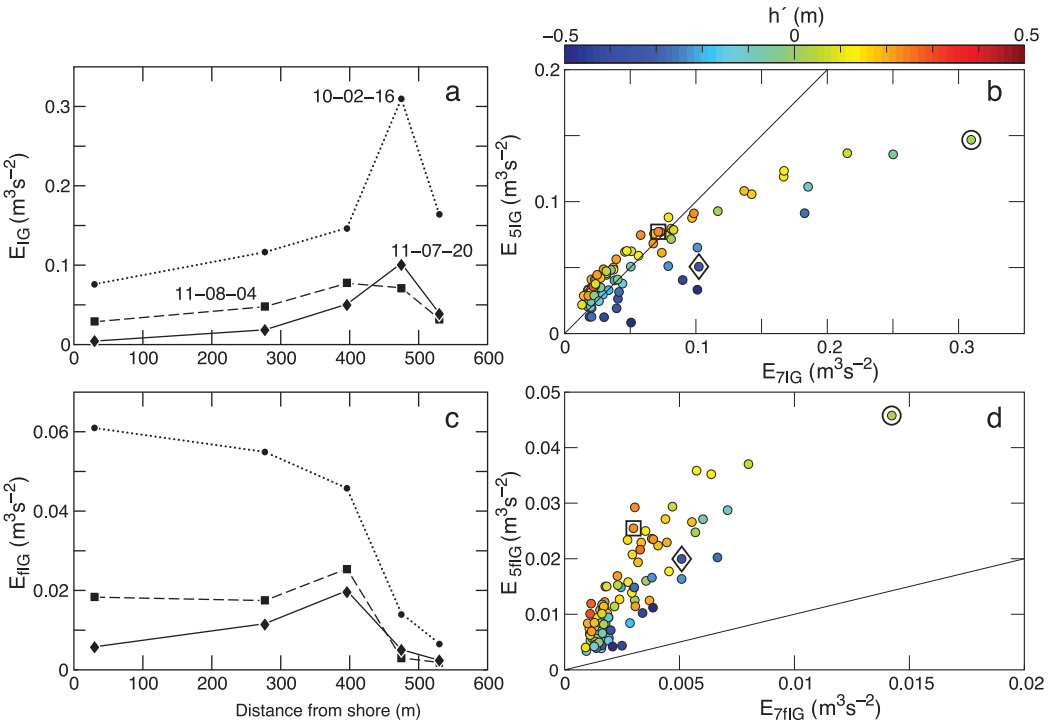

Figure 4. (a) Cross-shore variation of integrated IG energy for three wave events: 2 October 2009 (10-02-16, circles), 7 November (11-07-20, diamonds), and 8 November (11-08-04, squares). (b) Integrated IG band energy at sensor 7 versus sensor 5, colored with the tide h' defined as the detrended mean water level at sensor 8, for time periods when H_s at sensor 8 exceeds 1.5 m. The three wave events depicted in Figure 4a are labeled by their corresponding symbol. (c and d) Same as Figures 4a and 4b for the fIG band.

sensor location, except at the shoreline (sensor 1) where the flux is always near zero. The outgoing IG energy flux is prominent on the reef face (sensors 7 and 8) and at the shoreline (sensor 1), presumably due to partial (reef face) and near-complete (shoreline) wave reflections. The linear energy flux exhibits a tidal modulation on the reef flat (sensors 1, 3, and 5), which is particularly evident during the prolonged wave event in early November. The nonlinear flux is appreciable and directed offshore in opposition to the linear flux at the deepest reef face sensor 8, consistent with bound waves (i.e., maximum M and minimum ζ at SS group peaks). An increase in total IG energy flux (linear + nonlinear) occurs on the reef face (between sensors 7 and 8), with a marked decrease at the shoreward limit of the reef flat (sensor 5 compared to 7) for all large wave events.

While the fIG band fluxes (Figure 5b) share similar tendencies to the IG fluxes, notable differences are evident. In particular, the fIG linear flux increases appreciably between the reef face and outer reef flat (sensor 5 compared to 7), counter to the decreasing IG flux and similar to the fIG band energy. The linear flux at sensor 8 is weak compared to the nonlinear flux; however, the incoming and outgoing components of the linear flux are comparable in amplitude to the nonlinear flux. We interpret this as the signature of weak fIG bound wave energy present on the reef face with additional outgoing linear fIG flux, which is present at all sensors. We note that the fIG linear fluxes exhibit a tidal modulation on the reef flat similar to the IG fluxes.

A comparison of incoming and outgoing linear energy flux on the reef face and the outer reef flat (sensors 7 and 5, Figure 6) further illustrates the tidal influence on LF waves. A near linear relationship between incoming and outgoing IG (Figure 6a) and fIG (Figure 6c) fluxes on the reef face, without a strong tidal dependence (particularly for IG), suggests that LF wave reflections at the reef face are not strongly tidally modulated. The slope of the lines provides an approximate estimate of the degree of reflection in each band, 0.4 for IG and 0.5 for fIG, although we note that energy generated at the breakpoint may contribute to the outgoing flux. Our main conclusion with regard to wave reflections is that they cannot account for the observed tidal modulation of the transmitted energy on to the reef as measured at sensor 5. In the IG band, the incoming flux at 5 is always less than on the reef flat at 7 for all wave conditions, with relatively more flux occurring at high tide than low tide (Figure 6b). In contrast in the fIG band, the incoming flux at 5

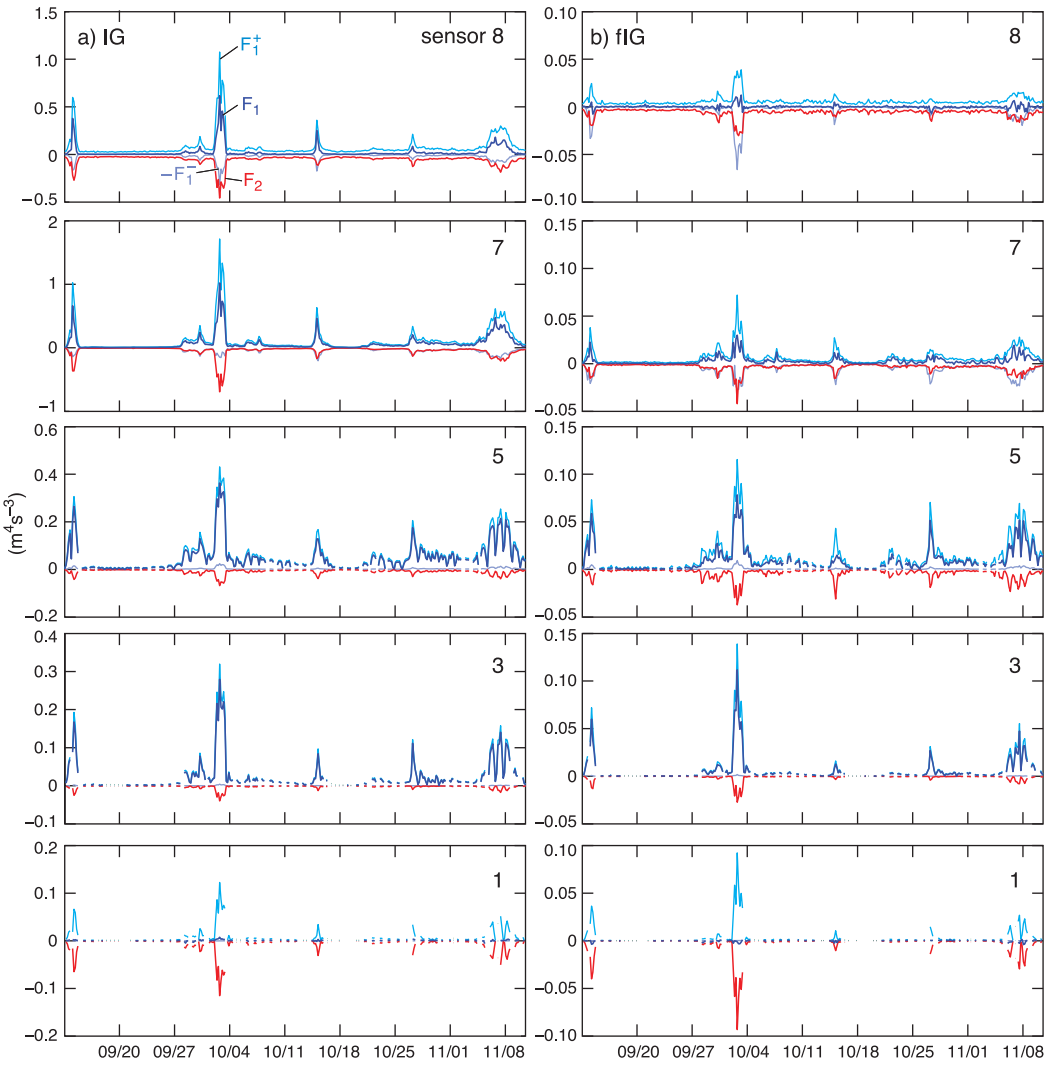

Figure 5. Time series of linear (F_1) and nonlinear (F_2) energy flux (2), integrated over the (left) IG and (right) fIG frequency bands, for each current-meter sensor location across the reef. The linear flux is further decomposed into incoming (F_1^+) and outgoing ($-F_1^-$) components according to (10).

is nearly always larger than the flux at 7, again with higher amplitudes at high tide than low tide. We will examine LF energy flux changes across the reef further in section 4.3.

4.2. Bound Waves

Bound waves are forced by radiation stress gradients and hence vary with the incoming SS group assuming small Ursell number and horizontally uniform statistics. In the IG band, cross spectra between the incoming surface elevation and the envelope of SS band elevation at sensor 8 show a near 180° phase difference, consistent with bound wave theory [*Longuet-Higgins and Stewart*, 1962]. Bispectral analysis has been used to describe variability associated with bound IG waves [*Hasselmann*, 1962; *Hasselmann et al*., 1963; *Herbers et al*., 1994]. *Herbers et al.* [1994] estimated bound wave energy levels by integrating bispectra of sea surface elevation over all SS wave pairs with difference frequencies in the LF band. They showed that bound wave energy increases quadratically with increasing incident SS wave energy, and that bound waves (and harmonics of the primary waves) are associated with biphase of 180° (0°), consistent with the theoretical phase locking of difference (and sum) triad interactions.

Here, we compute bispectra of sea surface elevation for the energetic wave event 10-02-16, which is representative of other SS wave events, to assess LF bound wave contributions at Ipan. On the reef face (sensor 8), statistically significant sum and difference-frequency interactions are detected from the bispectrum of

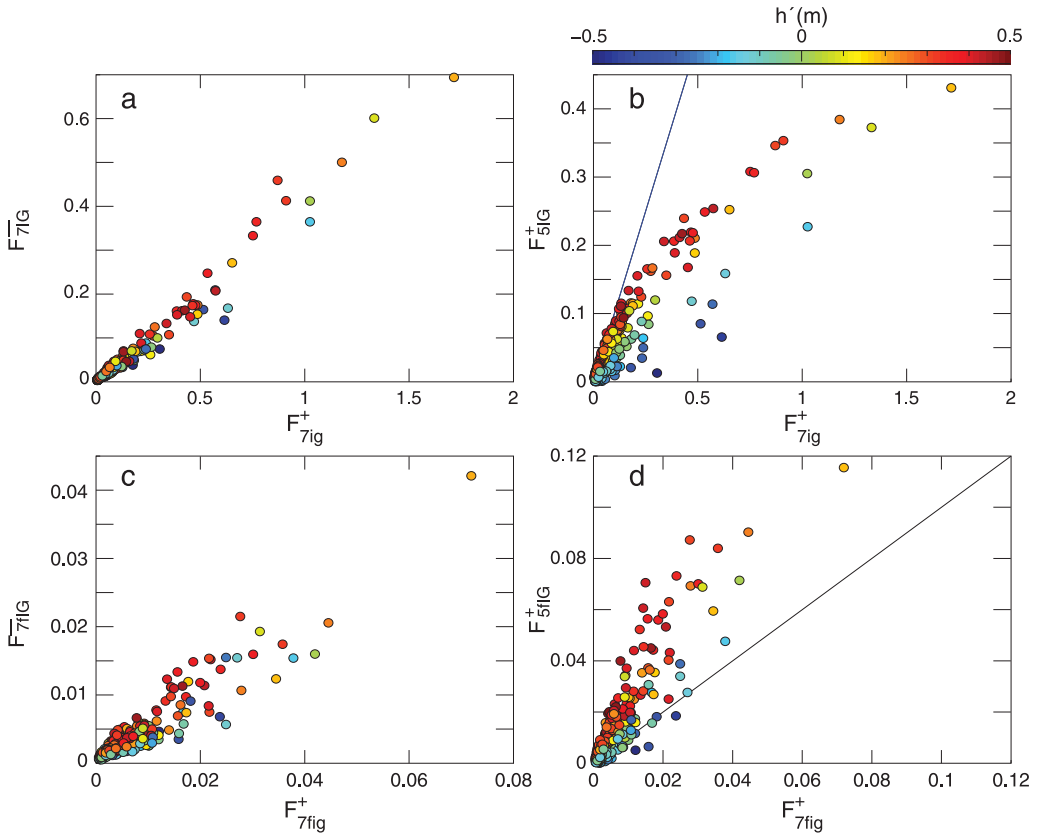

Figure 6. (a) The IG incoming linear flux at sensor 7 (F^{+}_{7IG}) versus the outgoing flux (F^{-}_{7IG}), colored with the tide h'. The least squares regression slope is 0.40 ± 0.04. (b) IG incoming linear flux at sensor 7 (F^{+}_{7IG}) versus sensor 5 (F^{+}_{5IG}). The line indicates a 1-to-1 relationship. (c) Regression slope is 0.52 ± 0.07, and (d) same as Figures 6a and 6b for the fIG band.

sea surface elevation (Figures 7a and 7b, difference interactions zone A, sum interactions zone B). Difference frequency interactions with ∼180° biphase (Figure 7c) are observed for SS band frequencies $f_1 \sim 0.07$ Hz and $f_3 \sim 0.08$ Hz and IG band frequency $f_2 \sim 0.01$ Hz, near a spectral peak in the power spectral density (Figure 7d). Sum interactions with near 0° biphase are observed for SS band frequencies f_1 and f_2 (Figure 7, zone B), and $f_3 \sim 0.16$ Hz near the first harmonic of the main SS peak visible in the power spectral density (Figure 7d).

The imaginary part of the bispectrum (Figure 7b) relates to the deviation of the biphase from 0 or 180° and provides a measure of the onshore growth or decay of energy flux due to triad interactions [*Norheim and Herbers*, 1998]. At sensor 8, the imaginary part of the bispectrum is positive for zone A, indicating onshore growth of IG energy from difference interactions. Negative values of the imaginary component for zone B suggest decay of the harmonics associated with sum interactions shoreward. Using *Herbers et al.* [1994] equations (5) and (6), and the sea surface elevation bispectrum at sensor 8, we estimate that the difference frequency interactions account for ∼87% of the IG spectral energy peak (Figure 7d), suggesting that IG band energy is predominantly due to forced bound waves formed in deep water that shoal and grow as near-resonant triads over the reef face. Approximately half of the relatively weak fIG energy at sensor 8 is due to difference interactions. Weak bound wave energy in the fIG band also was reported by [*Herbers et al.*, 1995] for observations at Duck, North Carolina.

Inshore of the surf zone (sensor 5), where the reef flat SS energy levels are weak, the bispectrum of sea surface elevation at all frequencies is much weaker than on the reef face (Figure 8a). The harmonics of the SS peak are no longer present in the sea surface elevation spectrum (Figure 8d) due to strong SS dissipation through the surf zone. The real part of the bispectrum at sensor 5 in zone A (Figure 8a) peaks at a lower frequency than the peak in the reef face bispectra (Figure 7a). The interactions among components in the swell, IG and fIG peaks have a near zero biphase (Zone A in Figures 8a and 8c), which we interpret as a

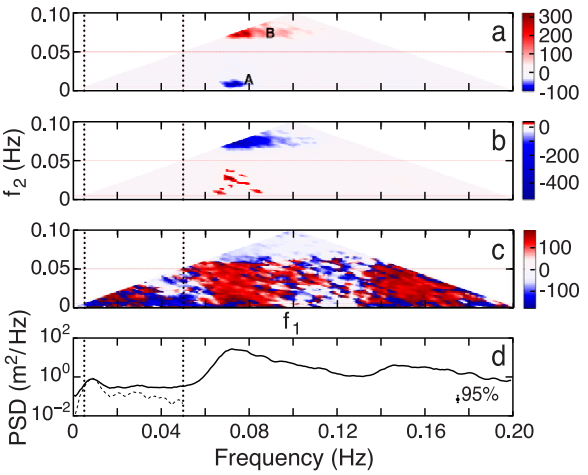

Figure 7. Bispectral estimate of sea surface elevation of the 2 October 2009 (10-02-16) at sensor 8. The (a) real and (b) imaginary parts of the bispectrum and the (c) biphase are shown with the corresponding power spectral density shown in Figure 7d, solid line. The bound wave contribution to the power spectral density also is shown (Figure 7d, dashed line). Zone A identifies the range of frequencies where difference interactions (biphase ~ 180°) between energetic SS waves and IG wave energy are significant. Zone B identifies the range of frequencies where sum interactions (biphase ~ 0°) between SS waves and SS harmonics are significant. Vertical dotted lines indicate the fIG and IG bands.

remnant of direct forcing of LF energy in the surf zone, primarily in the fIG band, by SS wave groups, similar to a varying breakpoint forcing [*Symonds et al.*, 1982; *Symonds and Bowen*, 1984; *Schäffer*, 1993]. In contrast to the reef face, difference interactions do not account for a significant fraction of the fIG band energy at sensor 5 (Figure 8d). We also note that the imaginary part of the bispectrum is partially negative in zone A at sensor 5 (Figure 8b), in contrast to the consistently positive values in this zone on the reef face (Figure 7b). This suggests some energy decay in the fIG band at sensor 5 [*Norheim and Herbers*, 1998].

4.3. Generation and Dissipation of LF Wave Energy

We consider the energy equation (5) to assess IG and fIG energy generation and dissipation across the reef in discretized form

$$d(F_1+F_2)=(\overline{W_1}-\bar{D})dx, \tag{12}$$

where the left-hand side is the difference between the combined linear and nonlinear energy fluxes between pairs of sensors separated by dx, $\overline{W_1}$ is the average nonlinear transfer (6), and $\bar{D}$ is the average dissipation due to bottom friction. The overbar denotes an equal-weighted average of the quantity measured at the sensor pair. In addition, we consider the alternative form of the nonlinear transfer for the sensors on either side of the surf break, sensors 5 and 7, using the discretized version of (5)

$$\overline{\hat{W}_1}\,dx=-gC_{\bar{U},dS_{xx}}. \tag{13}$$

The dissipation term, (11), requires specification of the drag coefficient c_f. For the outer reef sensor pairs (7 and 8, and 5 and 7), we use $c_f=0.02$, a low value for reef environments [*Van Dongeren et al.*, 2013]. On the reef flat, we apply a least squares fit to (11) and (12) to obtain c_f. We do not assess uncertainties for the terms in the energy budget as we do not know the errors involved in applying the discretized estimates in (12) and (13). We consider the relative importance of the estimated terms, but we do not attempt to close the energy budget.

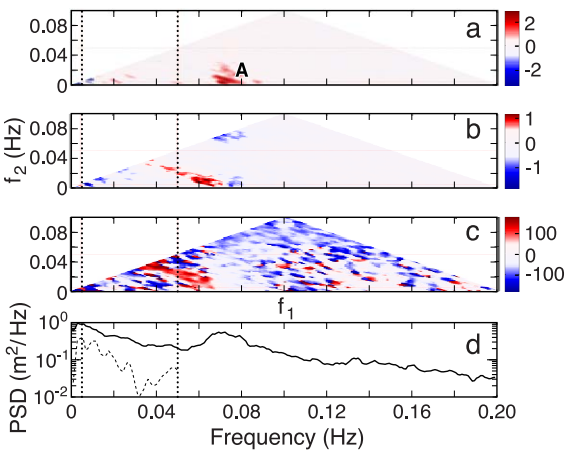

Figure 8. Same as Figure 7 but for sensor 5 on the reef flat. The difference interaction zone again is identified as zone A.

The band averaged energy terms on the reef face (between sensors 7 and 8) indicate that the increase in energy flux for both IG and fIG waves

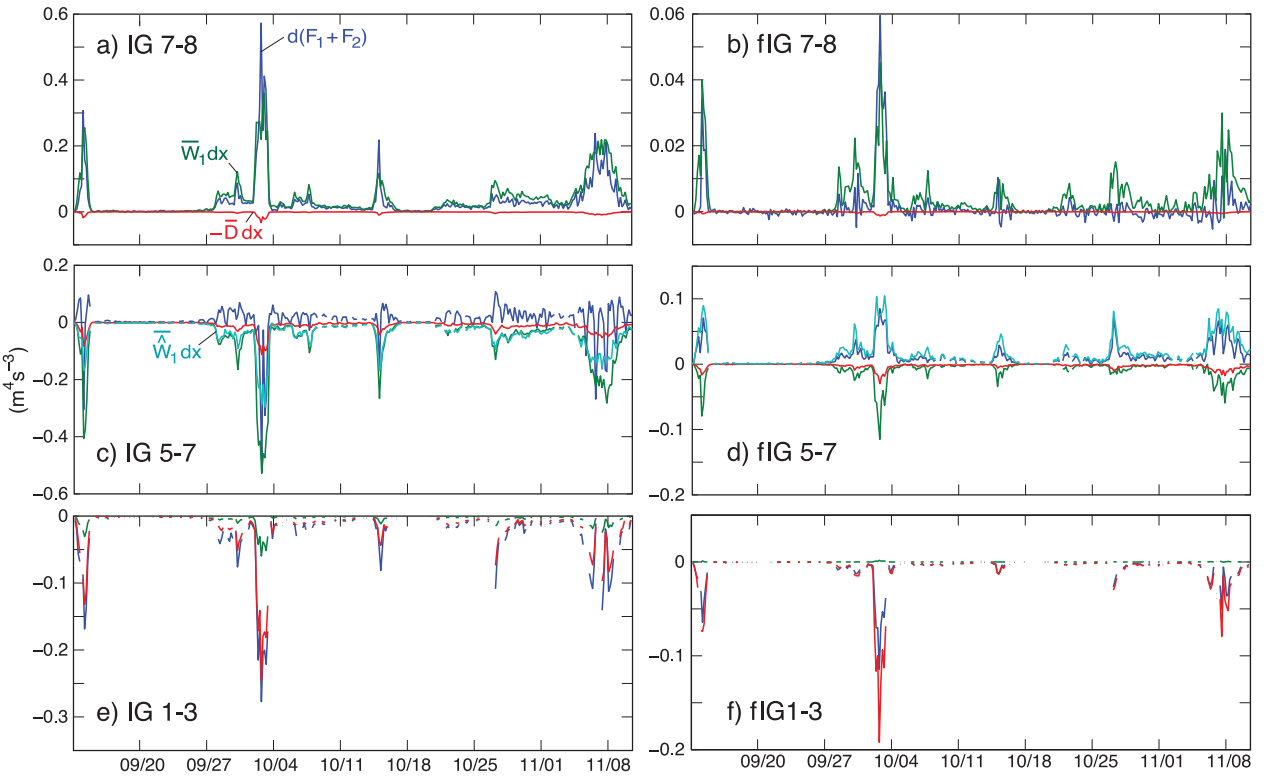

Figure 9. Time series of the flux divergence ($d(F_1+F_2)$), nonlinear conversion ($\overline{W}_1 dx$), and the bottom friction dissipation ($-\overline{D}dx$) in (12) evaluated for the sensor pair 7–8 on the reef face for the (a) IG and (b) fIG (bands. (c and d) Same as Figures 9a and 9b for the sensor pair 5–7, spanning the reef face and outer reef flat except that the alternative version of nonlinear conversion ($\overline{\hat{W}}_1$) is included. (e and f) Same as Figures 9a and 9b for the sensor pair 1–3 on the reef flat.

is accounted for primarily by nonlinear conversion (Figure 9). Dissipation appears to be negligible over the rugged reef face. A higher value of c_f may be appropriate, but there is no indication that an increased drag coefficient is required given the near balance between nonlinear conversion and flux divergence. Hence, incident SS waves provide a source of energy for IG and fIG waves as the SS waves shoal over the reef face.

Through the surf zone (between sensors 5 and 7), the reduction in IG energy flux is balanced primarily by nonlinear conversion, and to a lesser extent by bottom friction (Figure 9). Thus, as SS waves break near the reef crest, the radiation stress gradient works against the IG waves, which is a consequence of the near 180° phase difference between the SS wave envelope and the incident IG bound waves. We note that both estimates of the nonlinear conversion, (6) and (7), yield similar results for the IG band in this zone.

For the fIG band, the positive flux divergence is accounted for by the nonlinear conversion estimate, $\overline{\hat{W}_1}$, but not $\overline{W_1}$, which is of the opposite sign. We conclude that (13) captures the breakpoint forcing of fIG energy across the surf zone by specifying directly the radiation stress gradient, whereas the other conversion estimate (12) is evaluated outside of the main surf zone, and simple endpoint averages are not sufficient to resolve this energetic zone. Because fIG bound wave energy is weak over the reef face, fIG flux divergence is positive unlike the IG band. Although we do not have direct estimates of frictional dissipation, we find that bottom friction, with $c_f = 0.02$, contributes significantly to both IG and fIG decay in this transition region from reef face to reef flat.

We next consider whether the IG energy on the reef flat takes the form of a released bound wave [*Battjes et al.*, 2004], or a shoaling bound wave [*Pomeroy et al.*, 2012], by examining the lagged cross correlations between the SS wave envelope at sensor 8 and the IG band surface elevation at the various sensors. The lags of maximum cross correlation correspond to estimated travel times and group speeds ($\sqrt{gh}$) between sensors. The sign of the lagged cross correlation is negative over the reef face, consistent with bound waves, and positive for all sensors on the reef flat, consistent with breakpoint forced waves, similar to the observation of *Pomeroy et al.* [2012] for Ningaloo Reef. Thus, breakpoint generated IG waves dominate over released bound waves on the reef flat. We therefore interpret the IG energy flux reduction as the result of

nonlinear conversion working to diminish the incident bound waves, with additional work going into generating breakpoint forced free waves.

Similar to the linear flux comparisons depicted in Figure 6, the IG energy flux divergence between 5 and 7 exhibits a tidal dependence, with more IG energy transmitted onto the reef flat at high tide compared to low tide (Figure 9), with the tidal influence particularly evident during the prolonged wave event in early November. For high tides during weak to moderate wave conditions, the total IG energy flux divergence tends to be positive, which is due to the nonlinear flux divergence as the linear flux divergence is small at high tide (Figure 6). Neither the tidal dependence nor the positive flux divergence is accounted for by either estimate of the nonlinear conversion. Although dissipation exhibits a weak tidal dependence, an increased drag coefficient would not lead to better agreement with the flux divergence, moreover, dissipation cannot account for the positive flux divergence. In contrast, the nonlinear conversion term, $\overline{\hat{W}_1}$, (13), captures the tidal modulation of the flux divergence for the fIG band. We suspect that the lack of tidal dependence for the IG band is due to problems in resolving the nonlinear conversion at the spacing of the sensors 5 and 7. The conversion term depends on the phasing between radiation stress gradients and the IG cross-shore current (7). The changes in tidal height will affect IG wave propagation across the breaker zone, and faster propagation at high tide may lead to a more in phase relationship between U and $\frac{\partial S_{xx}}{\partial x}$ than at low tide. In addition, SS breaking may differ at high tide than low tide, resulting in larger radiation stress gradients at low tide. In general, the positive IG flux divergences between 5 and 7 (Figure 9c) arise due to the nonlinear flux divergence. The linear flux divergence (not pictured) is generally less than zero for all conditions and in better agreement with the combined conversion and dissipation terms depicted in Figure 9c than is the total flux divergence.

On the reef flat where SS waves are weak, bottom friction balances the decay in IG and fIG energy fluxes, which are nearly entirely linear (Figure 9). We use the sensor pair 1 and 3, noting that similar results are obtained using other sensor combinations on the reef flat. In the IG band, nonlinear conversion continues to draw energy from the IG waves moving across the reef; however, bottom friction is the dominant dissipation mechanism. A tidal variation in bottom friction dissipation also is evident with relatively higher dissipation during low than high tides. The range in the estimated c_f using different combinations of reef flat sensors is 0.008–0.018. For sensors 1–3, $c_f = 0.018 \pm 0.001$ (95% confidence intervals) for the IG band, and $c_f = 0.011 \pm 0.001$ for the fIG band.

4.4. Comparison With Conditions During Tropical Storm Man-Yi

During tropical storm Man-Yi in July 2007, fIG cross-shore standing modes were observed on Ipan reef, which appear to have been forced by low-frequency modulations of breaking waves during the peak of the swell event [*Péquignet et al*., 2009]. One measure of the standing pattern is the comparable incoming and outgoing fIG energy flux levels at the outer reef flat (sensor 5), suggesting nearly complete reflection and little energy loss as seen in Figure 10d. During Man-Yi, the standing modes are observed in the fIG frequency band; in the IG band the incoming energy flux is more than a factor of two larger than the outgoing flux (Figure 10b) suggesting partially standing waves and the influence of bottom friction dissipation. During the winter 2009 swell events, the outgoing energy flux at the outer reef flat (sensor 5) ranges from 10 to 30% of the incoming flux in the IG band, and 10 to 70% in the fIG band (Figures 10a and 10c).

The standing wave pattern indicated by the nearly equal incoming and outgoing outer reef fIG energy flux that occurred during Man-Yi is likely due to the higher water level over the reef flat compared to the winter 2009 events. At the peak of Man-Yi, the total water depth on the reef flat was almost 0.5 m deeper than at the peak of the largest winter 2009 event considered here, due to large wave setup and tidal elevation. The peaks of the winter 2009 events occurred during low tides (Figures 2a and 2d). The 0.5 m increase in reef flat water depth is estimated to decrease the frictional dissipation by 50% during Man-Yi compared to the largest winter 2009 wave events.

The presence of normal modes in the fIG frequency band during Man-Yi was demonstrated using an empirical orthogonal function (EOF) analysis of fIG sea surface elevation *Péquignet et al*. [2009]. An EOF analysis of the 2 October 2009 event (not shown) shows that similar to the Man-Yi event, 93% of the variance in the fIG band may be explained by the first two modes, with the spatial structure and time-dependent amplitudes consistent with normal mode excitation. In contrast to Man-Yi, however, for the 2 October 2009 event, the first normal mode (3/4 wavelength, 54% variance, modal period $T_1 \sim 235$ s, $f_1 \sim 0.0043$ Hz) is more

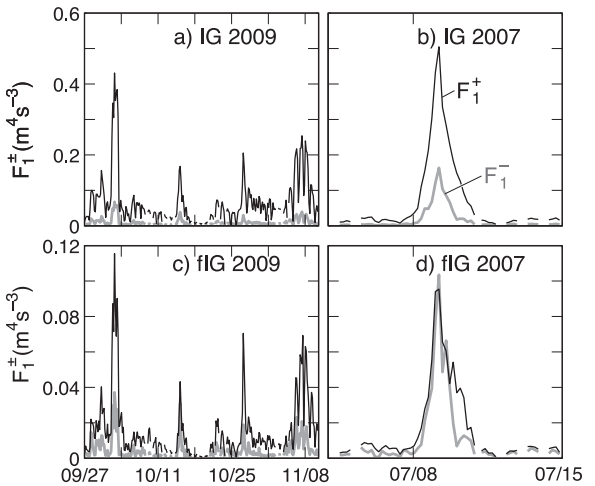

Figure 10. Time series of incoming (F_1^+ black) and outgoing (F_1^- gray) energy flux integrated over the (top) IG and (bottom) fIG frequency bands at sensor 5 on the outer reef flat for the (left) winter 2009 deployment, and (right) the deployment that included tropical storm Man-Yi.

energetic than the gravest normal mode (1/4 wavelength, 39% variance, $T_0 \sim 675$ s, $f_0 \sim 0.0015$ Hz) as the spectrum of the envelope of the SS free-surface elevation at sensor 8 is more energetic near the frequency of the first mode (Figure 11). The spectral distribution of the breakpoint forcing, as described by the spectrum of the envelope, favors the excitation of fIG energy, which dominates the LF energy at the shoreline. On the reef face prior to the breakpoint (sensor 8), the bound wave peak in the IG band is present, but not the fIG energy. The modal response in the fIG band further distinguishes it from the IG band. Both increased frictional dissipation and the work of bound waves against the breakpoint forced waves in the IG band favor the excitation of fIG rather than IG waves.

We remark that the LF elevation amplitudes at sensor 1 were slightly larger during the 2 October 2009 event than during the peak of Man-Yi. This likely is due in part to higher energy in the envelope at the mode 1 frequency during the 2 October 2009 event than the Man-Yi event. In addition, higher bound wave energy observed on the reef face during Man-Yi than 2 October 2009 potentially limited the breakpoint forcing of IG band energy. The quantitative prediction of the LF water level response at the shore requires a more comprehensive modeling approach than considered here, which takes into account variable breakpoint forcing, incident bound IG energy, and frictional dissipation that varies with water level, frequency, and cross-shore position.

5. Discussion and Conclusions

Field observations of LF wave transformation across a fringing reef are used to examine growth and decay of energy in the IG and fIG frequency bands. In particular, the energetics of the fIG frequency band has not received much attention in previous reef field studies. At IG frequencies, bound waves coupled to SS wave groups dominate the LF spectrum at the deepest reef face sensor (sensor 8), with considerably weaker fIG energy observed. On the steeply sloping reef face between sensors 8 and 7, nonlinear transfer leads to enhancement of energy in both the IG and fIG frequency bands. Incident SS waves break in a narrow surf zone, with considerable energy loss apparent within tens of meters from the reef edge (Figure 2a, sensors 5 and 6). Breaking results in strong, localized radiation stress gradients, modulated at low frequencies by SS wave groups that result in nonlinear energy transfer out of the IG band and a decrease in IG energy flux between the reef face and outer reef (Figure 9). The gains in IG energy flux in the shoaling region (Figure 9a) are largely lost in the break zone (Figure 9b). Energy dissipation due to bottom friction also likely contributes to LF wave decay. A similar nonlinear energy transfer from IG frequencies was described theoretically by *Schäffer* [1993], and has been reported in field observations on sandy beaches [*Henderson et al*., 2006; *Thomson et al*., 2006] in the absence of breaking. *Guedes et al*. [2013] reported that breaking SS waves on a dissipative beach caused a decrease in energy transfer to the IG band, and IG waves decayed as dissipation exceeded forcing. In addition, the numerical study of *Karunarathna and Tanimoto* [1995] on an idealized reef shows that incident wave group breaking causes the decay of bound waves. To date, on reefs, only growth of IG energy due to nonlinear transfer has been reported [*Pomeroy et al*., 2012]. Here we distinguish between the IG and fIG bands and find that positive nonlinear energy transfer into the fIG band and growth of fIG energy flux onto the reef flat is observed (Figure 3). During large wave events, fIG motions tend to be prominent at the lowest normal mode frequencies for the shallow, wide Ipan reef flat.

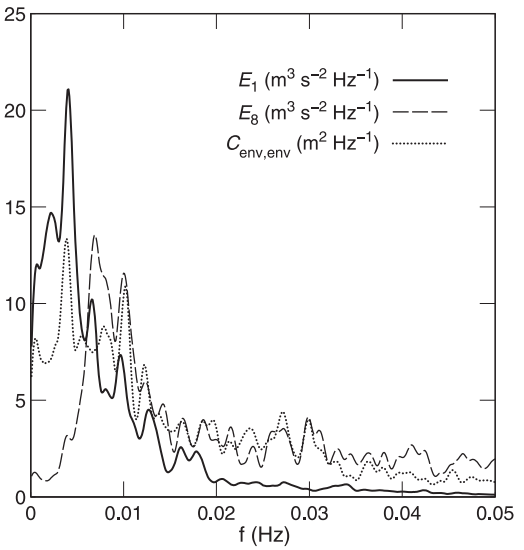

Figure 11. Energy density for the deepest reef face sensor (E_8), the reef flat sensor closest to shore (E_1), and the envelope of H_s at sensor 8, during the energetic wave event on 2 October 2009 (10-02-16).

The transformation of LF energy flux across the surf zone may be understood following the breakpoint forcing hypothesis of *Symonds et al*. [1982]. The incident bound waves result from nonlinear difference interactions within the SS frequency band, which generate phase-locked IG motions that are nearly 180° out of phase with the SS group as the waves approach the reef face. Breakpoint forcing may be interpreted as dynamic setup that generates long-waves in phase with the SS wave group at frequencies that are energetic in the SS envelope spectrum. The incident IG bound waves and breakpoint generated oscillations are near 180° out of phase, thus diminishing the incoming IG energy flux over the reef flat, with some locally generated energy remaining to propagate freely onto the reef flat. Thus, the bound waves do not appear to be released, at least not onto the reef flat, but replaced by a weaker locally forced response. In contrast, breakpoint forcing by the SS wave envelope, which is energetic in the fIG band (Figure 11), efficiently generates fIG waves in part because the fIG bound wave component is small.

Tidal dependence is observed in the energy flux on the reef flat for both IG and fIG bands, which we attribute to tidal modulation of nonlinear conversion and dissipation. Tidal dependence is not observed in the estimate of IG nonlinear transfer through the surf zone; however, we suspect that the sensor spacing is not suitable for resolving the details of the tidal influence on IG conversion in this energetic zone. Tidal modulation of IG energy transfer has been related to topographic concavity changes for sandy beaches [*Thomson et al*., 2006; *Guedes et al*., 2013]; such an effect would not pertain to reef flats like Ipan. We note that a tidal dependence also is observed in setup at Ipan [*Becker et al*., 2014]; however, the effect is the opposite to that on LF waves with higher setup at low tide than at high tide for a given incident wave height.

LF wave energy is observed to propagate shoreward across the reef flat, reflect in part at the shoreline, with bottom friction leading to wave decay. Based on regression fits of the energy flux divergence with the dissipation term, we estimate drag coefficients on the reef flat in the range of 0.008–0.018, which are weak compared to the LF values reported by *Pomeroy et al*. [2012] (0.06) and others, but not unexpected given the generally smooth, featureless reef flat at Ipan.

Our findings extend the work of *Pomeroy et al*. [2012], who examined the transformation of IG waves (0.004–0.04 Hz) over a fringing reef and lagoon at Ningaloo, Australia for moderate wave conditions ($H_{rms} < 1.6$ m). We consider the fIG frequency band, as well as the IG, for a reef without a lagoon under more energetic wave conditions (H_{rms} approaching 3 m). *Pomeroy et al*. [2012] found that the nonlinear energy flux was small (5–15%) and that bound waves generally were weak. For the more energetic conditions present at Ipan, we find that bound waves may account for 87% of the IG energy and that the nonlinear energy flux is comparable to the linear flux on the reef face during energetic events. In addition, *Pomeroy et al*. [2012] estimated nonlinear energy transfer over the reef flat but not the reef face or through the surf zone. They concluded that breakpoint forcing increased the IG energy flux through the surf zone, also confirmed in the numerical studies of *Van Dongeren et al*. [2013], whereas we find that breaking SS waves decrease the IG energy flux for energetic wave conditions. We suspect that the weaker wave conditions at Ningaloo led to weaker bound IG waves than at Ipan (bound waves scale as the incident SS wave height squared), and hence a net increase in IG band energy occurred as breakpoint forcing had less work to do against the weak bound waves.

In general, we find the balances for the energy equations encouraging, using reasonable estimates of bottom drag coefficients, even though the sensor array is sparse, particularly through the surf zone. Further progress can be made with higher spatial resolution measurements, which can be used to assess uncertainties of the energy terms. In particular, we were not able to estimate drag coefficients over the rugged spur and groove topography of the reef face or at the transition to the reef flat with the available data, although the estimated terms (between sensors 8 and 7) suggest that dissipation is relatively weak on the reef face. We emphasize that the main source of error in our analysis likely is associated with the estimate of the nonlinear transfer term, i.e., the specification of LF cross-shore velocity phase and amplitude relative to the radiation stress gradient. We note that the weakly nonlinear energy equation (1) results from slowly varying, depth-averaged dynamics [*Longuet-Higgins and Stewart*, 1962; *Henderson et al*., 2006] and as discussed in *Sheremet et al*. [2011]; the validity of these equations is questionable on a steep slope such as the reef face at Ipan. We also have neglected sources of dissipation, such as the possibility of LF wave breaking as suggested by *Van Dongeren et al*. [2013]. In addition, the Ipan reef face is porous, with observed flushing of water onto the reef flat through the reef infrastructure by breaking waves. The impact of this flushing on energy decay has not been considered.

As a result of the reduction of bound IG energy and the generation of fIG waves in the surf zone, LF energy at the Ipan shoreline has a spectral peak in the fIG band (Figure 3). The amplitude of the LF shoreline response depends not only on the SS envelope forcing amplitude but also its spectral structure and how it matches the normal mode frequencies. The observations of excitation of the gravest normal mode during tropical storm Man-Yi [*Péquignet et al*., 2009] and of a partially standing first mode during winter storms at Ipan highlight the excitation of normal reef modes by short wave groups and the frictional dissipation on the reef. This balance is influenced by water depth on the reef; higher water levels both will decrease frictional dissipation and favor the excitation of lower modes on fringing reefs like Ipan.

Acknowledgments

Field observations at Ipan, Guam were collected as part of the PILOT project, supported by the U.S. Army Corps of Engineers (USACE) via a subcontract from the University of California, San Diego. The PILOT project was led by Andrew Garcia and Stanley Boc (USACE). Additional support for analysis and manuscript preparation was provided by the National Science Foundation (OCE-0927407). Helpful discussions with Bob Guza, Jerome Aucan, Geno Pawlak, Chip Fletcher, Neil Frazer, and Doug Luther, and insightful comments from three anonymous reviewers are gratefully acknowledged. We thank Chris Kontoes and Carly Quisenberry, who directed the field experiments at Ipan, Anna Merrifield for assistance with the data processing, and Nancy Hulbirt for graphics support. The directional wave buoy data set was furnished by the Coastal Data Information Program (CDIP), Integrative Oceanography Division, operated by the Scripps Institution of Oceanography, under the sponsorship of the USACE and the California Department of Boating and Waterways. The meteorological data set from the Pago Bay tide gauge station was furnished by the NOAA Center for Operational Products and Services (CO-OPS). The current meter and pressure sensor data sets used in this study are available through the USACE at http://www.frf.usace.army.mil/pilot/pilot.shtml.

References

Baldock, T. E. (2012), Dissipation of incident forced long waves in the surf zone-implications for the concept of "bound" wave release at short wave breaking, *Coastal Eng.*, *60*, 276–285, doi:10.1016/j.coastaleng.2011.11.002.

Baldock, T. E., D. A. Huntley, P. A. D. Bird, T. O'Hare, and G. N. Bullock (2000), Breakpoint generated surf beat induced by bichromatic wave groups, *Coastal Eng.*, *39*, 213–242.

Battjes, J. A., H. J. Bakkenes, T. T. Janssen, and A. R. Van Dongeren (2004), Shoaling of subharmonic gravity waves, *J. Geophys. Res.*, *109*, C02009, doi:10.1029/2003JC001863.

Becker, J. M., M. A. Merrifield, and M. Ford (2014), Water level effects on breaking wave setup for Pacific Island fringing reefs, *J. Geophys. Res. Oceans*, *119*, 914–932, doi:10.1002/2013JC009373.

Boc, S., C. Pollock, A. Garcia, and J. Smith (2008), Typhoon inundation in an Island environment, *Solutions Coastal Disasters*, 276–287, doi:10.1061/40968(312)25.

Bowen, A. J., and R. T. Guza (1978), Edge waves and surf beat, *J. Geophys. Res.*, *83*(C4), 1913–1920.

Bricker, J. D., S. Munger, C. Pequignet, J. R. Wells, G. Pawlak, and K. F. Cheung (2007), ADCP observations of edge waves off Oahu in the wake of the November 2006 Kuril Islands tsunami, *Geophys. Res. Lett.*, *34*, L23617, doi:10.1029/2007GL032015.

Bryan, K. R., and A. J. Bowen (1996), Edge wave trapping and amplification on barred beaches, *J. Geophys. Res.*, *101*(C3), 6543–6552, doi:10.1029/95JC03627.

de Bakker, A. T. M., M. F. S. Tissier, and B. G. Ruessink (2014), Shoreline dissipation of infragravity waves, *Cont. Shelf Res.*, *72*, 73–82.

Demirbilek, Z., O. G. Nwogu, and D. L. Ward (2007), Laboratory study of wind effect on runup over fringing reefs. Report 1: Data report, *Tech. Rep. ERDC/CHL TR-07-4*, Coastal and Hydraul. Lab., Vicksburg, Miss.

Elgar, S., T. H. C. Herbers, and R. T. Guza (1994), Reflection of ocean surface gravity waves from natural beaches, *J. Phys. Oceanogr.*, *24*, 1503–1511.

Ford, M. R., J. M. Becker, and M. A. Merrifield (2013), Wave processes and excavation pits: Observations and implications for Majuro Atoll, Marshall Islands, *J. Coastal Res.*, *29*(3), 545–554.

Guedes, R., K. R. Bryan, and G. Coco (2013), Observations of wave energy fluxes and swash motions on a low-sloping, dissipative beach, *J. Geophys. Res. Oceans*, *118*, 3651–3669, doi:10.1002/jgrc.20267.

Guza, R. T., and E. B. Thornton (1982), Swash oscillations on a natural beach, *J. Geophys. Res.*, *87*(C1), 483–491.

Guza, R. T., and E. B. Thornton (1985), Observations of surf beat, *J. Geophys. Res.*, *90*(C2), 3161–3172.

Hardy, T. A., and I. R. Young (1996), Field study of wave attenuation on an offshore coral reef, *J. Geophys. Res.*, *101*(C6), 14,311–14,326, doi:10.1029/96JC00202.

Hasselmann, K. (1962), On the non-linear energy transfer in a gravity-wave spectrum, 1. General theory, *J. Fluid Mech.*, *12*, 481–500.

Hasselmann, K., W. Munk, and G. MacDonald (1963), Bispectra of ocean waves, in *Times Series Analysis*, edited by M. Rosenblatt, pp. 125–139, John Wiley, N. Y.

Henderson, S. M., and A. J. Bowen (2002), Observations of surf beat forcing and dissipation, *J. Geophys. Res.*, *107*(C11), 3193, doi:10.1029/2000JC000498.

Henderson, S. M., R. T. Guza, S. Elgar, T. H. C. Herbers, and A. J. Bowen (2006), Nonlinear generation and loss of infragravity wave energy, *J. Geophys. Res.*, *111*, C12007, doi:10.1029/2006JC003539.

Herbers, T. H. C., S. Elgar, and R. T. Guza (1994), Infragravity-frequency (0.005–0.05 Hz) motions on the shelf. Part 1: Forced waves, *J. Phys. Oceanogr.*, *24*, 917–927.

Herbers, T. H. C., S. Elgar, and R. T. Guza (1995), Generation and propagation of infragravity waves, *J. Geophys. Res.*, *100*(C12), 24,863–24,872.

Janssen, T. T., J. A. Battjes, and A. R. Van Dongeren (2003), Long waves induced by short-wave groups over a sloping bottom, *J. Geophys. Res.*, *108*(C8), 3252, doi:10.1029/2002JC001515.
Karunarathna, H., and K. Tanimoto (1995), Numerical experiments on low-frequency fluctuations on a submerged coastal reef, *Coastal Eng.*, *26*, 271–289.
Kench, P. S. (1998), Physical processes in a semi-enclosed Indian Ocean atoll, *Coral Reefs*, *17*, 155–168.
Lippmann, T. C., R. A. Holman, and A. J. Bowen (1997), Generation of edge waves in shallow water, *J. Geophys. Res.*, *102*(C4), 8663–8679.
Lippmann, T. C., T. H. C. Herbers, and E. B. Thornton (1999), Gravity and shear wave contributions to nearshore infragravity motions, *J. Phys. Oceanogr.*, *29*, 231–239.
Longuet-Higgins, M. S., and R. W. Stewart (1962), Radiation stress and mass transport in gravity waves, with application to "surf-beats," *J. Fluid Mech.*, *13*, 481–504.
Lowe, R. J., J. L. Falter, M. D. Bandet, G. Pawlak, M. J. Atkinson, S. G. Monismith, and J. R. Koseff (2005), Spectral wave dissipation over a barrier reef, *J. Geophys. Res.*, *110*, C04001, doi:10.1029/2004JC002711.
Lugo-Fernández, A., H. H. Roberts, W. J. Wiseman Jr., and B. L. Carter (1998), Water level and currents of tidal and infragravity periods at Tague Reef, St. Croix (USVI), *Coral Reefs*, *17*(4), 343–349, doi:10.1007/s003380050137.
Masselink, G. (1995), Group bound long waves as a source of infragravity energy in the surf zone, *Cont. Shelf Res.*, *15*(13), 1525–1547.
Monismith, S. G., L. M. M. Herdman, S. Ahmerkamp, and J. L. Hench (2013), Wave transformation and wave-driven flow across a steep coral reef, *J. Phys. Oceanogr.*, *43*, 1356–1379.
Nakaza, E., and M. Hino (1991), Bore-like surf beat in a reef zone caused by wave groups of incident short period waves, *Fluid Dyn. Res.*, *7*(2), 89–100, doi:10.1016/0169-5983(91)90062-N.
Norheim, C. A., and T. H. C. Herbers (1998), Nonlinear evolution of surface wave spectra on a beach, *J. Phys. Oceanogr.*, *28*, 1534–1551.
Nwogu, O., and Z. Demirbilek (2010), Infragravity wave motions and runup over shallow fringing reefs, *J. Waterw. Port Coastal Ocean Eng.*, *136*(6), 295–305, doi:10.1061/(ASCE)WW.1943-5460.0000050.
Oltman-Shay, J., and R. T. Guza (1987), Infragravity edge wave observations on two California beaches, *J. Phys. Oceanogr.*, *17*, 644–663.
Oltman-Shay, J., P. A. Howd, and W. A. Birkemeier (1989), Shear instabilities of the mean longshore current: 2. Field observations, *J. Geophys. Res.*, *94*(C12), 18,031–18,042.
Péquignet, A.-C., J. M. Becker, M. A. Merrifield, and J. Aucan (2009), Forcing of resonant modes on a fringing reef during tropical storm Man-Yi, *Geophys. Res. Lett.*, *36*, L03607, doi:10.1029/2008GL036259.
Péquignet, A.-C., J. M. Becker, M. A. Merrifield, and S. J. Boc (2011), The dissipation of wind wave energy across a fringing reef at Ipan, Guam, *Coral Reefs*, *30*, 70–82.
Phillips, O. M. (1977), *The Dynamics of the Upper Ocean*, 336 pp., Cambridge Univ. Press, N. Y.
Pomeroy, A., R. Lowe, G. Symonds, A. Van Dongeren, and C. Moore (2012), The dynamics of infragravity wave transformation over a fringing reef, *J. Geophys. Res.*, *117*, C11022, doi:10.1029/2012JC008310.
Raubenheimer, B., and R. T. Guza (1996), Observations and predictions of run-up, *J. Geophys. Res.*, *101*(C11), 25,575–25,587.
Roberts, H. H., P. A. Wilson, and A. Lugo-Fernandez (1992), Biologic and geologic responses to physical processes: Examples from modern reef systems of the Caribbean-Atlantic region, *Cont. Shelf Res.*, *12*(7), 809–834.
Ruessink, B. G. (1998), Bound and free infragravity waves in the nearshore zone under breaking and nonbreaking conditions, *J. Geophys. Res.*, *103*(C6), 12,795–12,805, doi:10.1029/98JC00893.
Ruggiero, P., R. A. Holman, and R. A. Beach (2004), Wave run-up on a high-energy dissipative beach, *J. Geophys. Res.*, *109*, C06025, doi:10.1029/2003JC002160.
Schäffer, H. A. (1993), Infragravity waves induced by short-wave groups, *J. Fluid Mech.*, *247*, 551–588.
Sheremet, A., R. T. Guza, S. Elgar, and T. H. C. Herbers (2002), Observations of nearshore infragravity waves: Seaward and shoreward propagating components, *J. Geophys. Res.*, *107*(C8), 3095, doi:10.1029/2001JC000970.
Sheremet, A., J. M. Kaihatu, S.-F. Su, E. R. Smith, and J. M. Smith (2011), Modeling of nonlinear wave propagation over fringing reefs, *Coastal Eng.*, *58*(12), 1125–1137, doi:10.1016/j.coastaleng.2011.06.007.
Stockdon, H. F., R. A. Holman, P. A. Howd, and A. H. Sallenger (2006), Empirical parameterization of setup, swash, and runup, *Coastal Eng.*, *53*(7), 573–588.
Suhayda, J. M. (1974), Standing waves on beaches, *J. Geophys. Res.*, *79*(21), 3065–3071, doi:10.1029/JC079i021p03065.
Symonds, G., and A. J. Bowen (1984), Interactions of nearshore bars with incoming wave groups, *J. Geophys. Res.*, *89*(C2), 1953–1959.
Symonds, G., D. A. Huntley, and A. J. Bowen (1982), Two-dimensional surf beat: Long wave generation by a time-varying breakpoint, *J. Geophys. Res.*, *87*(C1), 492–498, doi:10.1029/JC087iC01p00492.
Thomson, J., S. Elgar, B. Raubenheimer, T. H. C. Herbers, and R. T. Guza (2006), Tidal modulation of infragravity waves via nonlinear energy losses in the surf zone, *Geophys. Res. Lett.*, *33*, L05601, doi:10.1029/2005GL025514.
Van Dongeren, A., A. Reniers, J. Battjes, and I. Svendsen (2003), Numerical modeling of infragravity wave response during Delilah, *J. Geophys. Res.*, *108*(C9), 3288, doi:10.1029/2002JC001332.
Van Dongeren, A., J. A. Battjes, T. T. Janssen, J. van Noorloos, K. Steenhauer, G. Steenbergen, and A. Reniers (2007), Shoaling and shoreline dissipation of low-frequency waves, *J. Geophys. Res.*, *112*, C02011, doi:10.1029/2006JC003701.
Van Dongeren, A., R. Lowe, A. Pomeroy, D. M. Tranh, D. Roelvink, G. Symonds, and R. Ranasinghe (2013), Numerical modeling of low-frequency wave dynamics over a fringing coral reef, *Coastal Eng.*, *73*, 178–190.
Vetter, O., J. M. Becker, M. A. Merrifield, A.-C. Pequignet, J. Aucan, S. Boc, and C. Pollard (2010), Wave set-up over a Pacific Island fringing reef, *J. Geophys. Res.*, *115*, C12066, doi:10.1029/2010JC006455.